ARL-TR-10209 ● SEP 2025

Niobium-Containing Nanorods Grown by Reactive Sputtering

by Thomas C. Parker and Samuel G. Hirsch

NOTICES

Disclaimers

The findings in this report are not to be construed as an official Department of the Army position unless so designated by other authorized documents.

Citation of manufacturer's or trade names does not constitute an official endorsement or approval of the use thereof.

Destroy this report when it is no longer needed. Do not return it to the originator.

ARL-TR-10209 ● SEP 2025

Niobium-Containing Nanorods Grown by Reactive Sputtering

Thomas C. Parker and Samuel G. Hirsch
DEVCOM Army Research Laboratory

REPORT DOCUMENTATION PAGE

1. REPORT DATE	2. REPORT TYPE	3. DATES COVERED	
		START DATE	END DATE
September 2025	Technical Report	10/1/2024	9/10/2025

4. TITLE AND SUBTITLE
Niobium-Containing Nanorods Grown by Reactive Sputtering

5a. CONTRACT NUMBER	5b. GRANT NUMBER	5c. PROGRAM ELEMENT NUMBER
5d. PROJECT NUMBER	**5e. TASK NUMBER**	**5f. WORK UNIT NUMBER**

6. AUTHOR(S)
Thomas C. Parker and Samuel G. Hirsch

7. PERFORMING ORGANIZATION NAME(S) AND ADDRESS(ES)	8. PERFORMING ORGANIZATION REPORT NUMBER
DEVCOM Army Research Laboratory ATTN: FCDD-RLA-ME Aberdeen Proving Ground, MD 21005	ARL-TR-10209

9. SPONSORING/MONITORING AGENCY NAME(S) AND ADDRESS(ES)	10. SPONSOR/MONITOR'S ACRONYM(S)	11. SPONSOR/MONITOR'S REPORT NUMBER(S)

12. DISTRIBUTION/AVAILABILITY STATEMENT
DISTRIBUTION STATEMENT A. Approved for public release: distribution unlimited.

13. SUPPLEMENTARY NOTES
ORCID: Thomas Parker, 0000-0002-6151-6815

14. ABSTRACT
In this work, we explore the deposition of nanorods using oblique-angle deposition while reactively sputtering niobium (Nb) targets with varying CH_4 flow rates. X-ray diffraction and transmission electron microscopy showed that the highest flow rate, 4 standard cubic centimeters per minute (SCCM) CH_4, resulted in nanorods that were amorphous, followed by 3 SCCM showing a transition to crystalline NbC nanorods, with a final transition at 0.1-SCCM CH_4 forming nanorods with strained and highly oriented Nb crystallites. The lattice strain, 3.2%, is attributed to H interstitials. X-ray photoelectron spectroscopy (XPS) analysis indicated that, with the decreasing CH_4 flow rate, there was a corresponding increase in carbide content and reciprocal decrease in graphitic content, with approximately 2%–52% for the former and approximately 80%–21% for the latter. Also, XPS showed that, with respect to atomic composition and decreasing CH_4 flow rate, there was a decrease in carbon content, an increase in Nb content, and an increase in O content, measuring approximately 80%–20%, 15%–60%, and 12%–30%, respectively. The reduced O content is attributed to an increased growth rate and a gettering effect of excess carbon and H.

15. SUBJECT TERMS
Sciences of Extreme Materials, reactive sputtering, nanorod, niobium carbide, crystalline orientation, amorphous

16. SECURITY CLASSIFICATION OF:			17. LIMITATION OF ABSTRACT	18. NUMBER OF PAGES
a. REPORT	b. ABSTRACT	C. THIS PAGE		
UNCLASSIFIED	UNCLASSIFIED	UNCLASSIFIED	UU	17

19a. NAME OF RESPONSIBLE PERSON	19b. PHONE NUMBER *(Include area code)*
Thomas C. Parker	(240) 841-5831

STANDARD FORM 298 (REV. 5/2020)
Prescribed by ANSI Std. Z39.18

Contents

List of Figures

1. Introduction

The use of oblique-angle deposited films and sculptured films has been studied extensively.[1,2] There is a large body of work examining different deposition methods including thermal evaporation,[1,3–5] sputtering,[2,6–8] and e-beam evaporation.[9–12] There has also been work exploring the use of reactive sputtering deposition under oblique-angle deposition (OAD) conditions to grow ZnO,[13] TiZrN,[14] AlN,[15,16] SnO_2,[17] NiWO,[18] and TiO_2.[19] To date there has been no work examining reactive sputtering of OAD niobium (Nb) systems. In this report, we examine the effect that varying CH_4 flow rates has on the composition, crystallinity, and chemistry of Nb-containing nanorods.

2. Experimental

The depositions were conducted in a stainless-steel box-style vacuum chamber with interior dimensions of approximately 60 × 60 × 60 cm. The chamber door is O-ring sealed. The system was pumped with a turbo molecular pump backed with a multistage roots-style dry pump. Prior to conducting each deposition, the system was pumped down to a pressure of 1.0E-6 Torr or less, as measured via an ion gauge. Low vacuum during deposition was measured with a capacitance manometer with a full range of 100 mTorr. The manometer gauge was zeroed after each pump-down to ensure accuracy. A three-position gate valve was placed in the choke position to reduce conductance to the turbo pump during the depositions. The typical pressure during the substrate cleaning and depositions was between 0.6 and 1.5 mTorr. Gas flows were controlled via mass flow controllers. The total gas flow ranged from 4 to 8 standard cubic centimeters per minute (SCCM). The gases used were ultra-high-purity (UHP) argon (99.999% purity) and UHP CH_4 (99.99% purity). During substrate cleaning, a 13.56-MHz RF supply was used with 100 W applied to a modified 8-inch sputter cathode (magnets removed) with 3 mTorr of flowing argon (Ar). The substrate was biased with –120 V and cleaned for 1 h with a mean bias supply current of 10 mA. Each deposition was 180 min. During the depositions the Ar flow was fixed at 4 SCCM, while for each of the three samples the CH_4 was fixed at 0.1, 3, and 4 SCCM of CH_4. A 3-inch sputtering gun was used for the depositions and had a 0.25-inch-thick Nb target (99.95% purity). All depositions were conducted at a fixed power of 150 W and a throw distance of 40 cm. Samples were deposited on 3-inch silicon (100) wafers with a nominal thickness of 380 µm. The wafers were tilted at an oblique angle of 85° with respect to the sputtering target surface.

To identify crystalline phases, X-ray diffractograms were acquired with a Bruker D8 X-ray diffractometer with a sealed Cu tube oriented in line focus. A Gobel optic was used to provide a parallel beam comprised of K α1 and K α2 followed by a 2.5° Soller slit. A linear silicon strip detector, with a 2.5° Soller slit, was operated in 1D mode with an energy resolution of less than 380 eV and an angular coverage of approximately 2°. All samples were measured over a 2θ scan range of 15° to 80°.

To determine composition and chemical state of the films, a PHI Versa Probe II was used to acquire X-ray photoelectron spectroscopy (XPS) spectra. The system was equipped with a monochromated Al X-ray source and samples were charge neutralized with a combination of a low-energy electron flood gun and a low-energy Ar ion beam. All samples were sputter cleaned at 1 keV for 10 min prior to XPS data acquisition. The high-resolution XPS scans were conducted with a pass energy of 26 eV and a step size of 0.05 eV.

A JEOL JEM-2100F at 200 kV was used for transmission electron microscopy (TEM) analysis. Samples were prepared by scraping the sample surface with a razor blade into 20 mL of isopropyl alcohol in a glass vial. The vial was capped and sonicated in a water bath for 10 min. A pipette was then used to withdraw a small amount of the suspension and a small droplet was placed on a 3-mm-diameter lacey carbon grid and allowed to evaporate. Samples were then imaged in the TEM using bright field and selected area diffraction.

3. Results and Discussions

In Figure 1, the C1s XPS data is shown for the 4 SCCM CH_4 flowrate in a), 3 SCCM in b), and 0.1 SCCM in c). In Figure 1a, the lowest binding energy peak at 282.87 eV is attributed to NbC and the peak at 284.8 eV is attributed to the C–C bond, that is, graphitic carbon. The remaining two peaks at 286.46 and 288.48 eV are attributed to the C=O and C–O bonds, respectively. In Figures 1b and 1c, a similar peak deconvolution is used. One apparent change is the relative height of the carbide peak as the CH_4 flow is changed. For the highest CH_4 flow, we see a carbide bond percentage of 1.84%, for the 3-SCCM sample it is 14.64%, and for the lowest flow rate the carbide is 51.94%. This is expected as the increased carbon content with flowrate would naturally lead to C–C bonds as there are an insufficient number of Nb atoms arriving on the rod surface to bond with carbon.

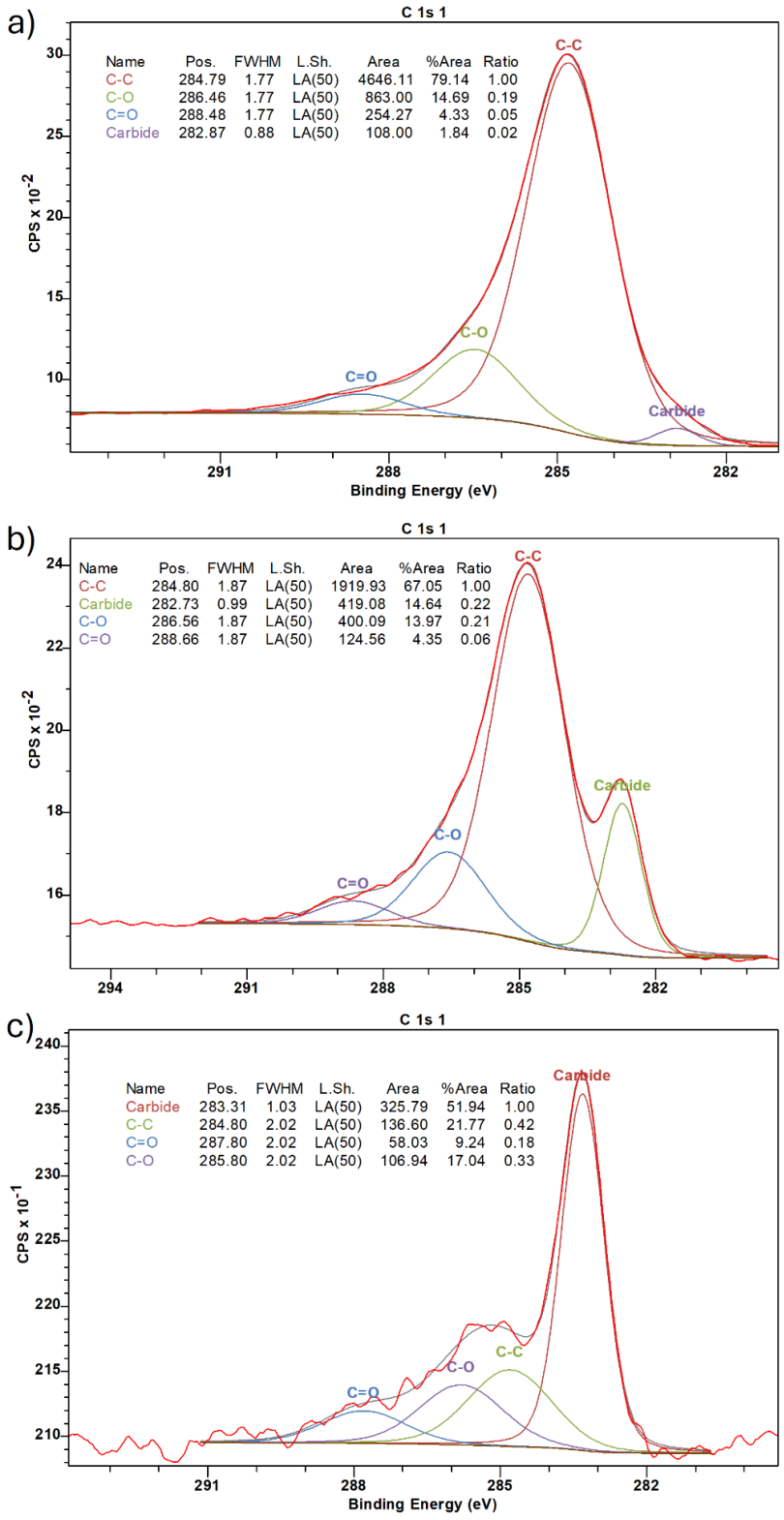

Figure 1. High-resolution XPS of C1s peaks for different flows of CH_4 a) 4 SCCM, b) 3 SCCM, and c) 0.1 SCCM.

In Figure 2a, the XPS composition for the films shown in Figure 1 are shown with the addition of the data from both a 1-SCCM and a 2-SCCM CH_4 sample. As the CH_4 flow is increased, the percentage of carbon increases. Also of note is that the percentage of oxygen decreases with increasing CH_4 flow. This can be attributed to two effects: one is the increased growth rate of the nanorods with increased CH_4 flow rate leads to less incorporation of residual oxygen in the vacuum chamber, and the second is that excess carbon and hydrogen from the CH_4 decomposition act as getters forming volatile oxygen compounds such as H_2O and CO/CO_2, which are then subsequently pumped away.

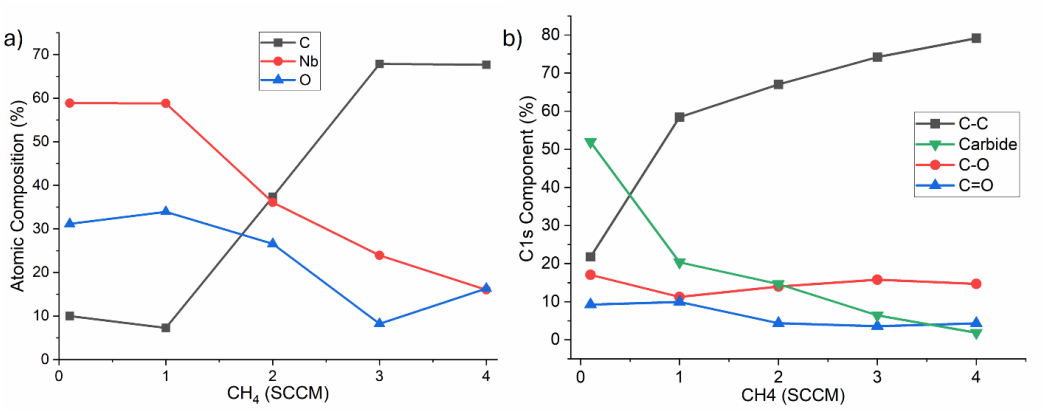

Figure 2. a) Atomic composition vs. CH_4 flow, and b) the percent of the deconvolution peaks of C1s vs. CH_4 flow rate.

In Figure 3, TEM micrographs are shown for the 4-, 3-, and 0.1-SCCM samples. In Figure 3a, on the left is a bright-field (BF) image of the nanorods grown with 4 SCCM, and on the right is the selected area diffraction (SAD) pattern of the same. The BF image shows the nanorods were scraped off in bundles. The base of the nanorods start from the lower right direction running diagonally to the upper left of the image. In the SAD pattern, the nanorods show no apparent crystallinity and appear amorphous in nature. In Figure 3b, the CH_4 flow rate during nanorod growth was 3 SCCM. In the BF image on the left, the nanorod bundle in the center is nearly vertical in orientation with the base of the nanorods at the bottom. On the right, the SAD pattern clearly shows some diffraction rings indicating the nanorods are crystalline. Additionally, there are some bright spots as well as partial breaks in the rings indicating some crystalline texture and orientation. The diffraction pattern agrees with that of NbC. Finally, in Figure 3c the sample with the lowest CH_4 flow of 0.1 SCCM is shown. The BF image on the left shows the tips of three nanorods where the base of the nanorods start out of the frame, off to the left. The SAD pattern on the right clearly indicates a very strong crystalline texture that can be attributed to Nb.

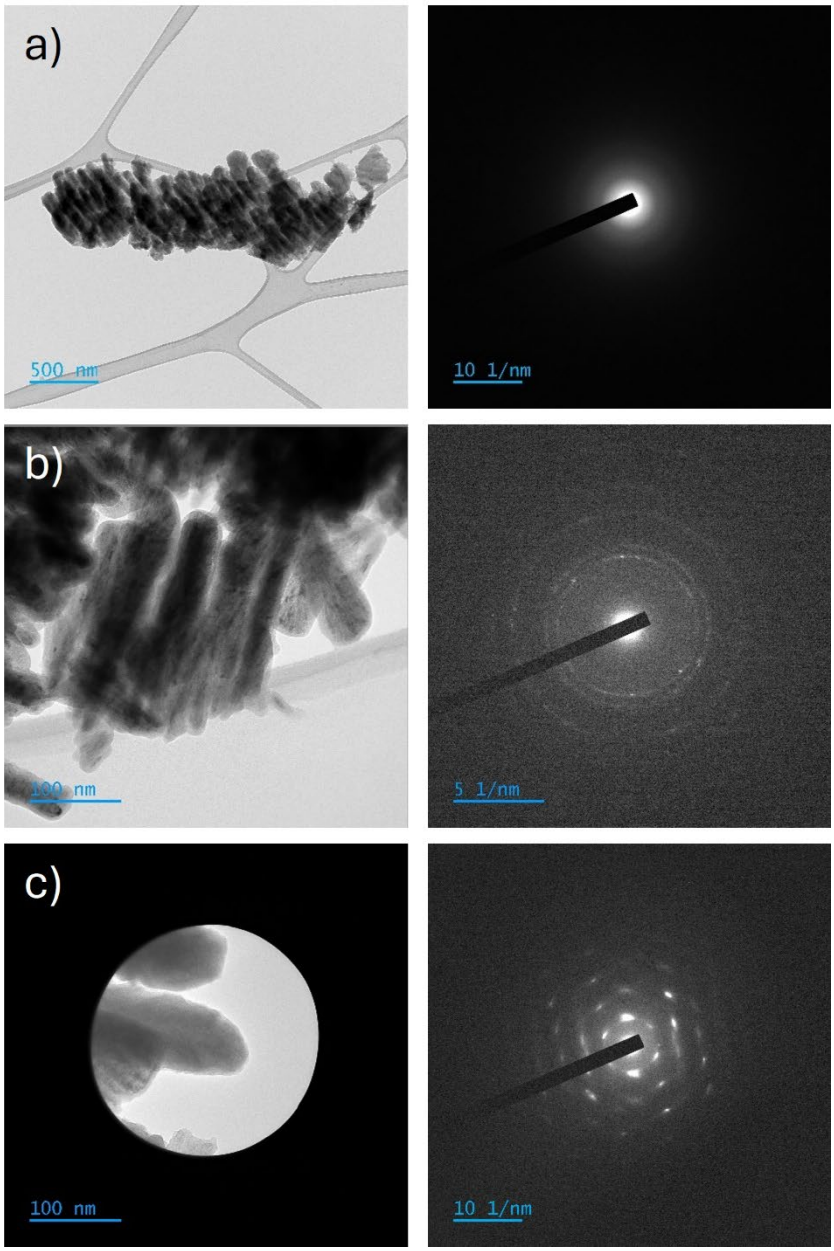

Figure 3. a) BF (left) and SAD (right) of sample with 4-SCCM CH_4 flow, b) BF (left) and SAD (right) of sample with 3-SCCM CH_4 flow, and c) BF (left) and SAD (right) of sample with 0.1-SCCM CH_4 flow.

In Figure 4, the X-ray diffraction (XRD) data for the nanorods with the three flow rates are shown. All samples in Figure 4 showed evidence of a glassy and amorphous peak centered at 20°. This peak was attributed to the amorphous graphitic carbon phase for all three samples as indicated by the vertical dashed line. In Figure 4a, the XRD data for the sample with the 4-SCCM flow rate is shown. The only feature of note is the amorphous graphitic phase. Otherwise, the film

appears to be amorphous in nature in agreement with the SAD pattern in Figure 3a. In Figure 4b, the presence of a crystalline phase is demonstrated by the appearance of peaks. These peaks are relatively broad, which can be due to compositional gradients with the crystallites, nanocrystallites, inhomogeneous strain, or a combination thereof. The peaks are readily indexed to NbC and in agreement with the SAD pattern shown in Figure 3b. Finally, in Figure 4c the sample with the lowest CH_4 flow at 0.1 SCCM is shown. The diffraction data again indicates a crystalline material with narrower peaks (vs. Figure 4b). The sample was indexed as Nb with a lattice strain of 3.2%. This lattice strain cannot be due to the typical thin film effects. Whereas, in a typical thin film, the substrate can deform the film due to a continuous bond interface. In this case, the free-floating nanorod crystallite strain is more likely caused by interstitial lattice inclusions. We suspect these interstitials are H. Further studies using in-situ heated XRD would help to determine if this lattice strain dissipates at low temperatures less than 380° C, the decomposition temperature of Nb hydride.

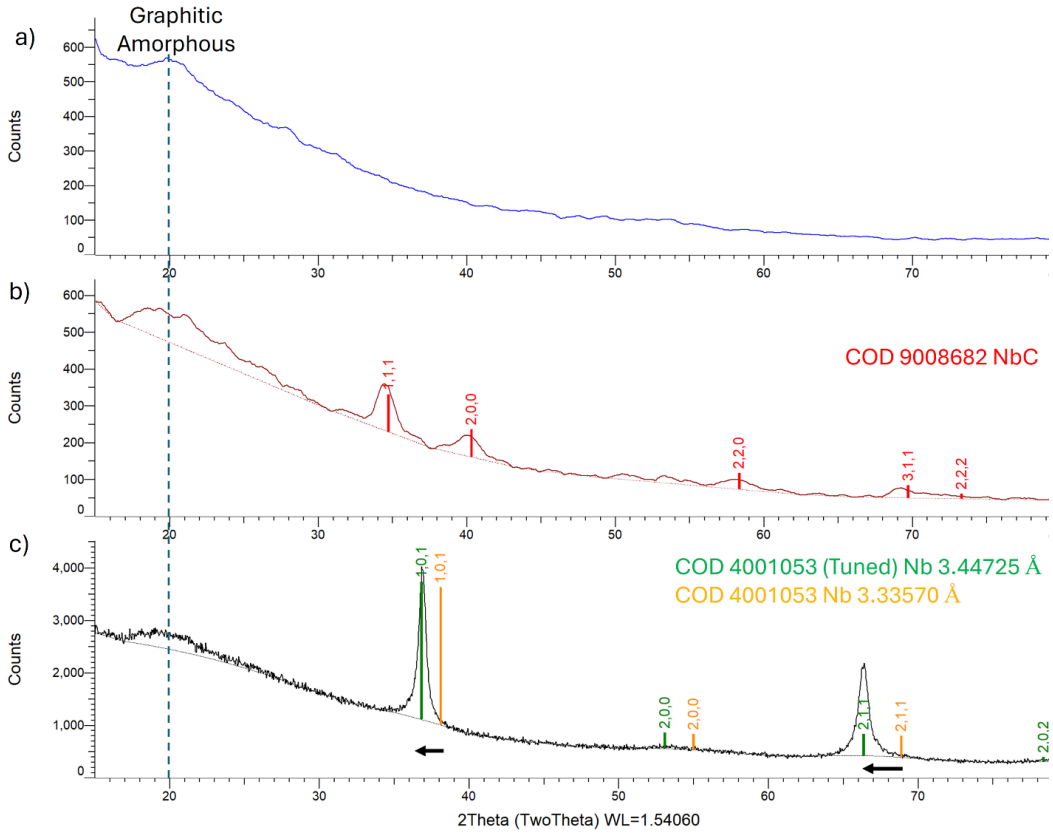

Figure 4. XRD scans of as-deposited nanorod samples. a) 4-SCCM flow rate, b) 3-SCCM flow rate, and c) 0.1-SCCM flow rate.

4. Conclusion

We have demonstrated the growth of reactively sputtered nanorods. The XPS data showed that with decreasing CH_4 flow the graphitic carbon decreased and the carbide phase increased. Conversely, the oxygen in the nanorods also decreased with increased CH_4 flow, likely due to increased nanorod growth rate and a gettering effect of excess carbon and H. With decreasing CH_4 flow, the nanorods change from an amorphous nature (4 SCCM) to a crystalline NbC (3 SCCM) and finally ending with a strained highly textured Nb (0.1 SCCM) crystalline state. Further work examining annealing may help to determine if interstitial atoms such as H are responsible for the lattice strain seen in the lowest CH_4 flow rate sample.

5. References

1. Tang F, Parker T, Li HF, Wang GC, Lu TM. The Pd catalyst effect on low temperature hydrogen desorption from hydrided ultrathin Mg nanoblades. Nanotechnology. 2008;19:465706.
2. Teki R et al. Nanostructured silicon anodes for lithium-ion rechargeable batteries. Small. 2009;5:2236–2242.
3. Licausi N et al. Bhat, growth of CdTe films on amorphous substrates using CaF_2 nanorods as a buffer layer. J Electron Mater. 2009;38:1600–1604.
4. Morrow P, Tang XT, Parker TC, Shima M, Wang GC. Magnetoresistance of oblique angle deposited multilayered Co/Cu nanocolumns measured by a scanning tunnelling microscope. Nanotechnology. 2008;19:065712.
5. Gaire C et al. Small angle grain boundary Ge films on biaxial CaF_2/glass substrate. J Crystal Growth. 2010;312:607–610.
6. Krishnan R, Parker T, Lee S, Lu TM. The formation of vertically aligned biaxial tungsten nanorods using a novel shadowing growth technique. Nanotechnology. 2009;20:465609.
7. Shetty AR, Karimi A, Cantoni M. Effect of deposition angle on the structure and properties of pulsed-DC magnetron sputtered TiAlN thin films. Thin Solid Films. 2011;519:4262–4270.
8. Ghekiere P, Mahieu S, De Gryse R, Depla D. Structure evolution of the biaxial alignment in sputter-deposited MgO and Cr. Thin Solid Films. 2006;515:485–488.
9. Wang P-I, Parker TC, Karabacak T, Wang GC, Lu TM. Size control of Cu nanorods through oxygen-mediated growth and low temperature sintering. Nanotechnology. 2009;20:085605.
10. Wang S et al. Structural and optical properties of nanostructured TiO_2 thin films fabricated by glancing angle deposition. J Alloys Compd. 2007;431(1–2):287–291. https://doi.org/10.1016/j.jallcom.2006.05.091
11. Brown T, Robbie K. Observations of self-assembled microscale triangular-shaped spikes in copper and silver thin films. Thin Solid Films. 2013;531:103–112.
12. Schmidt D et al. Optical, structural, and magnetic properties of cobalt nanostructure thin films. J Appl Phys. 2009;105:113508. https://doi.org/10.1063/1.3138809

13. Toledano D, Galindo RE, Yuste M, Albella JM, Sánchez O. Compositional and structural properties of nanostructured ZnO thin films grown by oblique angle reactive sputtering deposition: effect on the refractive index. J Phys D Appl Phys. 2013;46.

14. Phae-ngam W et al. Oblique angle deposition of nanocolumnar TiZrN films via reactive magnetron co-sputtering technique: the influence of the Zr target powers. Curr Appl Phys. 2019;19(8):894–901. https://doi.org/10.1016/j.cap.2019.05.002

15. Bairagi S et al. Glancing angle deposition and growth mechanism of inclined AlN nanostructures using reactive magnetron sputtering. Coatings. 2020;10.

16. Patidar J et al. Improving the crystallinity and texture of oblique-angle-deposited AlN thin films using reactive synchronized HiPIMS. Surf Coat Technol. 2023;468:129719.

17. Oros C et al. Ultra-sensitive NO_2 sensor based on vertically aligned SnO_2 nanorods deposited by DC reactive magnetron sputtering with glancing angle deposition technique. Sens Actuators B Chem. 2016;223:936–945. https://doi.org/10.1016/j.snb.2015.09.104

18. Jetjamnong C et al. Growth and characterization of NiWO nanorod films prepared by reactive magnetron co-sputtering with oblique angle deposition. Vacuum. 2022;196.

19. Alvarez R et al. High-rate deposition of stoichiometric compounds by reactive magnetron sputtering at oblique angles. Plasma Process Polym. 2016;13:960–964.

List of Symbols, Abbreviations, and Acronyms

1D	one-dimensional
AlN	aluminum nitride
Ar	argon
ARL	Army Research Laboratory
BF	bright field
CH_4	methane
CO	carbon monoxide
CO_2	carbon dioxide
DEVCOM	U.S. Army Combat Capabilities Development Command
H_2O	water
Nb	niobium
NiWO	nickel tungstate
OAD	oblique-angle deposition
RF	radio frequency
SAD	selected area diffraction
SCCM	standard cubic centimeters per minute
SnO_2	tin(IV) oxide
TEM	transmission electron microscopy
TiO_2	titanium dioxide
TiZrN	titanium-zirconium nitride
UHP	ultra-high purity
XPS	X-ray photoelectron spectroscopy
XRD	X-ray diffraction
ZnO	zinc oxide

1 (PDF)	DEFENSE TECHNICAL INFORMATION CTR DTIC OCA
1 (PDF)	DEVCOM ARL FCDD RLB CI TECH LIB